Chemical Science

EDGE ARTICLE

View Article Online
View Journal | View Issue

Cite this: *Chem. Sci.*, 2018, **9**, 7210

All publication charges for this article have been paid for by the Royal Society of Chemistry

An "all-in-one" antitumor and anti-recurrence/metastasis nanomedicine with multi-drug co-loading and burst drug release for multi-modality therapy†

Ji-Chun Yang,[a] Yue Shang,[b] Yu-Hao Li,[b] Yu Cui[a] and Xue-Bo Yin *[ac]

Received 25th May 2018
Accepted 29th July 2018

DOI: 10.1039/c8sc02305k

rsc.li/chemical-science

Drug-loading often suffers from tedious procedures, limited loading efficiency, slow release, and therefore a low curative effect. Cancer easily recurs and metastasizes even after a solid tumor is removed. Herein, we report a simple strategy with multi-drug co-loading and burst drug release for a high curative effect and anti-recurrence/metastasis. CuS nanoparticles, protoporphyrin IX, and doxorubicin were added to the precursors of ZIF-8 with one-pot co-loading during the formation of ZIF-8 for chemo-, photothermal-, and photodynamic-therapy to eliminate solid tumors. Negative CpG, as a kind of immune adjuvant, was adsorbed on the positive surface of ZIF-8 to inhibit the recurrence and metastasis of tumors with its long-term immune response. Precision treatment with one-pot multi-drug co-loading, controllable drug delivery, and multi-modality therapy may be anticipated by this versatile strategy.

Chemotherapy is popular because of its high curative effect and diversity of drugs.[1] Phototherapy, including photodynamic therapy (PDT) and photothermal therapy (PTT), has attracted much attention owing to the advantages of remote controllability, target selectivity, fewer side effects, and minimal invasiveness.[2–5] Each treatment has its own advantages, and multi-modality therapy provides a synergistic effect and is thus urgently required.[6,7] The design of a versatile platform and strategy to integrate multiple probes and agents according to clinical needs is critical to eliminate primary solid tumors.

Metal–organic frameworks (MOFs) are the hybrid of organic ligands and metal nodes, and their porous structure facilitates the integration of diverse species.[8,9] However, the adsorption-loading strategy is often tedious and multi-drug co-loading systems are still limited. We have loaded two drugs in core–shell MOF composites, where one was loaded in the core and the other in the shell with a multi-step procedure.[1] NO gas and metronidazole were co-loaded in HKUST-1, which was first activated thermally and then exposed to a dry methanol solution of metronidazole.[10] The metronidazole-loaded HKUST-1 was further activated at 80 °C under vacuum before being exposed to 2 atm of NO gas for NO adsorption. MIL-88A was soaked in the solution mixture of irinotecan and floxuridine for their co-loading, but the loading capacity of irinotecan decreased obviously compared to that of irinotecan alone.[11] Moreover, slow drug release leads to low drug concentration at the site of interest and thus a poor curative effect. The design of the system with high loading efficiency, a simple procedure, and fast drug release becomes essential for improving the curative effect for solid tumors.[12–14]

Recurrence and metastasis of tumors often occur after chemo- and photo-therapy ablate solid tumors effectively, because they are ineffective against metastatic cancer cells. Most patients have a low survival rate just because of cancer recurrence/metastasis risk.[15] Immunotherapy activates the individual's immune system.[16–18] Unmethylated cytosine-phosphate-guanine (CpG) oligonucleotides, as immune adjuvants, are recognized by Toll-like receptor 9 (TLR9) of the host cells and thus induce an immune response to produce Th1 and a proinflammatory cytokine. The immune-stimulating activity of CpG makes it attractive for application in immunotherapy.[19,20]

Herein, we propose a versatile one-pot strategy to integrate multiple probes and agents into one nanomedicine with burst drug release for traditional and immune combination therapy (Scheme 1). ZIF-8 is a class of MOFs with high surface area, nanoscale size, uniform pore structure, and simple preparation,[21] so it is selected as a platform to load multiple drugs. CuS nanoparticles (NPs) for PTT, protoporphyrin IX (PpIX) for PDT, and doxorubicin (DOX) for chemotherapy were added to the precursors of ZIF-8 to verify the capacity of ZIF-8 to load

[a]*State Key Laboratory of Medicinal Chemical Biology, Tianjin Key Laboratory of Biosensing and Molecular Recognition, College of Chemistry, Nankai University, Tianjin, 300071, China. E-mail: xbyin@nankai.edu.cn; Fax: +86-22-23503034*

[b]*Tianjin Key Laboratory of Tumor Microenvironment and Neurovascular Regulation, School of Medicine, Nankai University, Tianjin, 300071, China*

[c]*Collaborative Innovation Center of Chemical Science and Engineering (Tianjin), Nankai University, Tianjin, 300071, China*

† Electronic supplementary information (ESI) available: All experimental details, crystallographic data collection and refinement statistics, details of chemical synthesis, additional figures and tables. See DOI: 10.1039/c8sc02305k

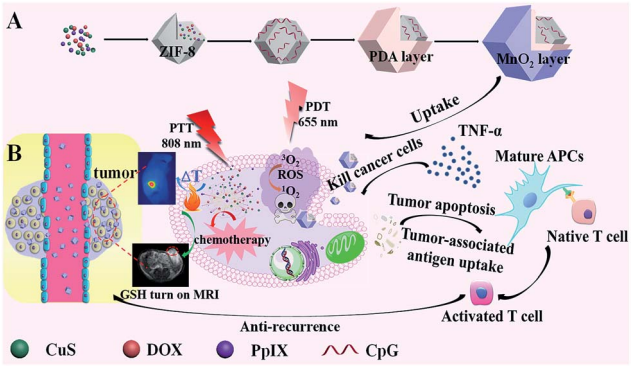

Scheme 1 (A) Preparation of the "all-in-one" nanocomposite. CuS nanoparticles, protoporphyrin IX, and doxorubicin were added to the precursors of ZIF-8 during its preparation to realize multi-drug co-loading, while negative CpG was adsorbed on the positive surface of ZIF-8. (B) Theranostic strategy using the nanocomposite for elimination of primary solid tumors with the synergic effect of PTT, PDT, and chemotherapy. CpG inhibited the recurrence and metastasis of tumors by the long term immune memory.

multiple probes and agents. CuS NPs also triggered burst drug release under NIR irradiation with their high photothermal conversion efficiency. The synergistic treatment and burst drug release eliminated the solid tumor efficiently. Negative CpG was also easily wrapped on the positive surface of ZIF-8 through electrostatic interaction for immunotherapy, which inhibited the recurrence/metastasis risk obviously. A polydopamine (PDA) layer enhanced the PTT effect, acted as a platform for the growth of MnO_2, and preserved the immune activity of CpG. $KMnO_4$ was added dropwise into CuS@ZIF-8@PDA (CuZP, the abbreviations of all the composites are provided in ESI Table S1†). MnO_2 nanosheets formed uniformly on the surface of the composites through the reaction between $KMnO_4$ and PDA to form CuZPMn for glutathione (GSH) "turn-on" magnetic resonance (MR) imaging. Thus, immunotherapy was integrated into this ZIF-8 based nanostructure to form an "all-in-one" system with MR imaging-guided chemotherapy, PDT, and PTT to realize both anti-tumor and anti-recurrence/metastasis.

Results and discussion

Design and characterization of the multi-modality therapy system

CuS nanoparticles (NPs), protoporphyrin IX (PpIX), and doxorubicin (DOX) were co-loaded in ZIF-8 by adding the NPs and agents in the precursors of ZIF-8 during its preparation for PTT, PDT, and chemotherapy. Moreover, CuS NPs were also used to trigger burst drug release under NIR irradiation with their high photothermal conversion efficiency. Negative CpG was wrapped onto the positive surface of ZIF-8 through electrostatic interaction for immunotherapy. A polydopamine (PDA) layer enhanced the PTT effect and also acted as a platform for the growth of MnO_2 and protection of the immune activity of CpG. $KMnO_4$ was added dropwise into the CuS@ZIF-8@PDA solution, so MnO_2 nanosheets formed uniformly through the reaction between $KMnO_4$ and PDA. The efficiency of the designed "all-in-one" system was confirmed with its anti-tumor and anti-recurrence/metastasis application.

CuS NPs were first used as a model to validate the efficiency of the one-step loading strategy during the preparation procedure of ZIF-8. The morphology of 3 nm CuS, 100 nm CuS@ZIF-8 (CuZ), 115 nm CuZP (polydopamine@CuZ), and 125 nm CuZPMn (MnO_2 nanosheet@CuZP) is clearly illustrated in their transmission electron microscopy (TEM) images with a uniform and monodisperse nature (Fig. 1A–D). CuS NPs were well dispersed in ZIF-8 to form CuZ nanocomposites (NCs) (inset of Fig. 1B). Moreover, the morphology of ZIF-8 remained stable after the loading of CuS NPs, indicating the ability of ZIF-8 to encapsulate various species. The surface of CuZ NCs became rough after being coated with the PDA layer to yield CuZP NCs. The uniform PDA layer improved the hydrophilic nature of the composite and protected CpG from deactivation by $KMnO_4$. The *ca.* 10 nm MnO_2 layer was clearly observed in CuZPMn NCs after the redox reaction between $KMnO_4$ and PDA. Dynamic light scattering results revealed that all the NCs had a relatively narrow size distribution for real applications (ESI Fig. S1A–D†).

The peaks at 29.3°, 31.0°, 48.0°, and 59.1° in the powder X-ray diffraction (XRD) patterns were assigned to the (102), (103), (110), and (116) planes of hexagonal phase CuS (JCPDS no. 06-0464) (Fig. 1E). The peaks observed at 7.3°, 12.7°, 18.0°, and 26.7° corresponded to the (011), (112), (222), and (134) planes of crystalline ZIF-8.[1] The relatively weak peaks at 36.6° and 65.6° matched well with those of α-MnO_2 (JCPDS no. 44-0141). CuZP showed a similar XRD pattern to CuZ because of the amorphous PDA structure. All the characteristic diffraction peaks of CuS, ZIF-8, and MnO_2 appeared simultaneously in CuZPMn NCs and confirmed the successful preparation of the NCs without altering the crystallinity of the ingredients. Thermogravimetric analysis (TGA) revealed the content of different ingredients in CuZPMn (Fig. 1F). The mass ratios of CuS, ZIF-8, PDA and MnO_2 in CuZPMn NCs were 7.6%, 37.1%, 37.0% and 18.4%, respectively, calculated from the 9.7% weight loss for CuS, 53.9% for CuZ, 74.7% for CuZP, and 61.1% for CuZPMn. The TGA result was consistent with the ICP-AES one listed in ESI Table S2.† All the elements, including Cu, Zn, Mn, C, N, O and S, were observed in the X-ray photoelectron spectroscopy (XPS) full

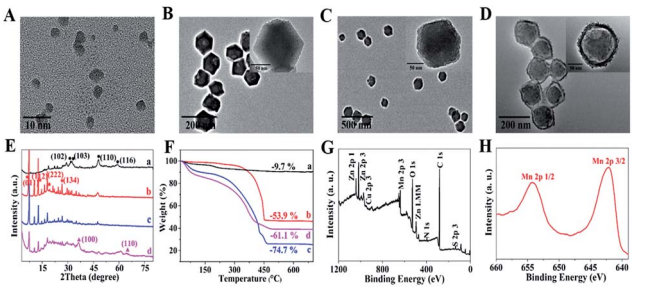

Fig. 1 TEM images of (A) CuS, (B) CuZ, (C) CuZP, and (D) CuZPMn (inset: the enlarged TEM images). (E) XRD patterns and (F) TGA of (a) CuS, (b) CuZ, (c) CuZP, and (d) CuZPMn. (G) XPS spectrum of CuZPMn and (H) high-resolution Mn 2p XPS spectrum (Cu, Z, P, and Mn in CuZPMn represent CuS, ZIF-8, polydopamine, and MnO_2, respectively. The abbreviations are also listed in ESI Table S1†).

spectrum of CuZPMn (Fig. 1G). The two peaks centered at 642.5 and 654.0 eV were assigned to Mn 2p3/2 and Mn 2p1/2 for MnO_2 (Fig. 1H).

N_2 adsorption–desorption isotherms were recorded to investigate the surface areas and pore size distributions of CuZ and CuZP NCs (ESI Fig. S2A and B†). Compared with ZIF-8, the surface area and pore volume of CuZ decreased from 0.49 $cm^3\ g^{-1}$ and 1560.0 $m^2\ g^{-1}$ to 0.23 $cm^3\ g^{-1}$ and 1153.4 $m^2\ g^{-1}$ because of the introduction of non-porous CuS NPs in ZIF-8. The surface area and pore volume of CuZP further decreased to 0.11 $cm^3\ g^{-1}$ and 274.5 $m^2\ g^{-1}$ after being coated with the PDA layer. The pyknotic PDA layer may serve as a platform for MnO_2 growth and a gatekeeper to prevent drug leakage before arriving at cancer sites.

The solvent-stability of CuZPMn NCs, as a key criterion for their practicability, was investigated by soaking them in distilled water, phosphate-buffered saline (PBS), and 10% fetal bovine serum (FBS) over 7 days. As shown in ESI Fig. S3,† no macroscopic aggregate or precipitate was observed, and the sizes of CuZPMn NCs in different solvents remained unchanged after storing them for 7 days. The high stability of CuZPMn NCs suggests their significant potential for *in vitro* and *in vivo* therapeutic applications.

In vitro drug loading and NIR-triggered release properties

PpIX, DOX, and CpG were further selected as models to evaluate the multi-drug loading capacity of CuZPMn NCs. A simple one-pot strategy was used to integrate CuS NPs, PpIX, and DOX into the internal part of ZIF-8 during its preparation. CpG was wrapped on the surface of ZIF-8 through electrostatic interaction. The zeta potentials of the products at each step were recorded to verify the successful preparation of different NCs. The zeta potential of CuZ@PpIX/DOX decreased dramatically after loading CpG, indicating that negative CpG was already attached onto the surface of ZIF-8 (ESI Fig. S4†). The drug-loading efficiencies were calculated to be approximately 94% for PpIX, 92% for DOX, and 98% for CpG based on a UV-Vis spectrum method (ESI Fig. S5 and S6†). The drug-loading capacity of DOX was about 20% (ESI Fig. S6†), which was higher than that of many other drug delivery systems.[22–24] The high multi-drug loading efficiency was achieved with the excellent encapsulation capacity of ZIF-8, strong π–π stacking, hydrogen bond, and electrostatic interaction between negatively charged DNA and positively charged ZIF-8.[25,26] Moreover, the one-pot drug-loading method achieved the encapsulation of PpIX and DOX in the internal part of ZIF-8 simultaneously, facilitating multi-drug loading with high capacity and a simple procedure.

DOX was used as a model to study the drug-release profile. Without NIR irradiation, as little as 2.8%, 7.6% and 23.2% of DOX were released under different pH conditions (pH 5.0, 6.5, and 7.4) after 12 h. However, 5 min of NIR laser irradiation (808 nm, 2 W cm^{-2}) before each determination led to the burst release of 58.6%, 63.9% and 71.2% of DOX in 4 h, respectively (Fig. 2A). Therefore, the slow and uncontrollable drug-release of traditional drug-carriers was easily improved with the NIR-triggered switch

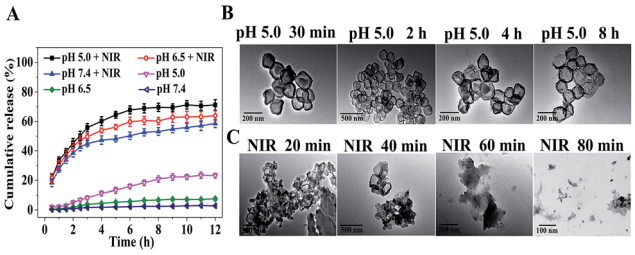

Fig. 2 (A) The release profiles of DOX from CuZPMn@DOX at pH 7.4, 6.5 and 5.0 with and without 808 nm laser irradiation (2 W cm^{-2}). TEM images of CuZPMn@DOX at (B) pH 5.0 from 30 min to 8 h and (C) different NIR irradiation time periods from 20 to 80 min at pH 5.0.

of CuZPMn@DOX, leading to an increase in the drug content in solid tumor sites for a high curative effect. TEM images of CuZPMn revealed the drug-release mechanism. Under acidic conditions (pH 5.0), the acid-unstable ZIF-8 core melted gradually, while the PDA and MnO_2 shell remained stable, as revealed by the hollow and circular structure observed in Fig. 2B. The drugs were retained in the composites with PDA and MnO_2 layers serving as a "gatekeeper". However, the edge became ambiguous and the composites degraded at pH 5.0 once NIR-stimulus irradiation was introduced (Fig. 2C). CuZPMn@DOX disintegrated rapidly because of the local hyperthermia of the CuS NPs and PDA layer, which acted as hot-spots with their excellent photothermal conversion ability.[1,27]

Photodynamic and photothermal properties

The *in vitro* photodynamic properties and photothermal performance of the nanocomposites (NCs) were tested (Fig. 3). To investigate the PDT capacity of the NCs, a solution containing 50 μg mL^{-1} CuZPMn@PpIX NCs and 100 μM ABDA was irradiated for 60 min with a 655 nm laser at a power intensity of 0.3 W cm^{-2}. The PDT ability of PpIX was well retained even when PpIX was embedded in the NCs, so light-triggered CuZPMn@PpIX NCs were considered to be a suitable candidate for PDT (Fig. 3A and B). The reactive oxygen species (ROS) generating capability of CuZPMn, CuZP@PpIX and CuZPMn@PpIX under 655 nm laser irradiation was also determined at the cell level using ROS-sensitive probe 2′,7′-dichlorofluorescin diacetate (DCFH-DA) (ESI Fig. S7†). As expected, visible intracellular ROS generation was observed after the introduction of PpIX into the NCs and 655 nm laser irradiation, which also confirmed the PDT ability of the NCs. Furthermore, the light-triggered ROS generation capability of CuZPMn@PpIX was remarkably enhanced compared with that of CuZP@PpIX because of the production of O_2 from endogenous H_2O_2 in tumors by MnO_2.[28,29] The UV-Vis-NIR spectra of CuZPMn were remarkably enhanced in a concentration-dependent manner, indicating its high light absorption capacity (Fig. 3C). The temperature increased with increasing NC concentration and irradiation time (Fig. 3D), demonstrating the potential of CuZPMn as a photothermal agent. The infrared thermal image illustrated the photothermal capacity of CuZPMn *in vitro* intuitively (Fig. 3E). For the *in vivo* PTT study, tumor-bearing mice

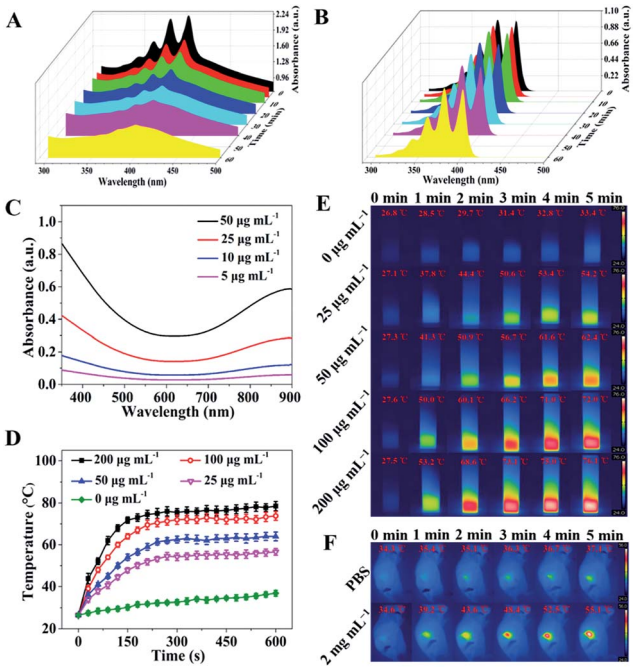

Fig. 3 UV absorbance spectra of 100 μM ABDA in the (A) presence and (B) absence of 50 μg mL^{-1} CuZPMn@PpIX under irradiation at 655 nm at different time periods. (C) UV-Vis-NIR absorbance spectra of CuZPMn NPs. (D) Photothermal heating curves of CuZPMn under 808 nm laser irradiation at 2 W cm^{-2} for 10 min. (E) *In vitro* and (F) *in vivo* infrared thermal photographs of PBS and CuZPMn recorded at different time intervals when exposed to 808 nm laser irradiation.

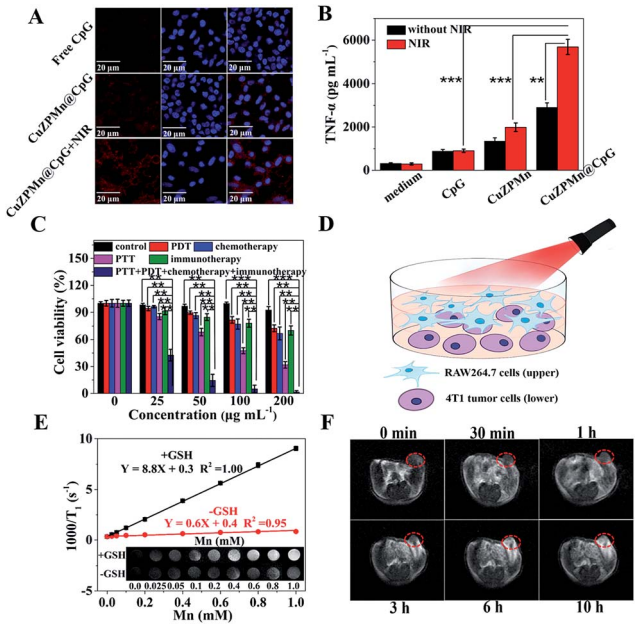

Fig. 4 (A) Confocal fluorescence images of RAW264.7 cells treated with free CpG, CuZPMn@CpG, and CuZPMn@CpG after NIR irradiation. (B) The secretion of TNF-α from RAW264.7 cells stimulated with different treatments. (C) Cell viabilities of 4T1 cells treated with different treatments. (D) Schematic illustration for immunotherapy. RAW264.7 cell (upper) and 4T1 tumor cell (bottom) co-cultured Transwell system for mimicking the *in vivo* tumor model. RAW264.7 cells incubated with CuZPMn@CpG were subjected to NIR for 3 min to trigger the release of CpG. (E) *In vitro* GSH-responsive T_1-weighted MRI of CuZPMn (inset: T_1-weighted images of CuZPMn at different Mn concentrations with and without GSH). (F) T_1-weighted MR images of tumor-bearing mice before and after intravenous injection of CuZPMn.

were exposed to 808 nm laser irradiation for 10 min at 10 h post-intravenous injection of CuZPMn (Fig. 3F). The temperature of tumor sites increased rapidly to higher than 55 °C for the perfect tumor ablation. Damage to normal tissues was avoided owing to their low temperature achieved by simple control of the laser. Thus, CuZPMn was found to be an efficient photothermal agent for PTT and NIR-triggered drug release simultaneously with single NIR irradiation.

Study of the intracellular uptake and immune response of CuZPMn@CpG

CpG is easily recognized by the mammalian immune system through TLR9 in endolysosomes.[30] Therefore, the internalization of CpG into antigen presenting cells is important to induce an immune response.[31] Cellular uptake of CuZPMn NCs was first quantified by Mn content per cell through inductively coupled plasma mass spectrometry (ICP-MS) detection (ESI Fig. S8†). Both RAW264.7 and 4T1 cells presented high cellular uptake efficiencies (approximately 72% for RAW264.7 and 78% for 4T1) of CuZPMn NCs. The efficiency of CuZPMn@CpG uptake by RAW264.7 cells was also recorded with confocal fluorescence imaging after CpG was labeled with red-emission Cy5. Thus, the co-localization of CpG-nano-composites was revealed by confocal fluorescence imaging of the red emission of Cy5. No apparent fluorescence was observed in cells treated with free CpG (Fig. 4A). Negative CpG may be degraded by nucleases or/and hardly ingested by RAW264.7 cells because of the electrostatic barrier of the cytoplasmic membrane.[32] However, bright fluorescence was observed in the cytoplasm of RAW264.7 cells after being incubated with CuZPMn@CpG, indicating that CuZPMn@CpG NCs exhibited much better cellular uptake efficiency and crossed the cell membrane easily. Moreover, the fluorescence was remarkably enhanced after 808 nm irradiation, indicating that a large amount of CpG accumulated in cells owing to the improved membrane permeability after NIR irradiation.[19] Thus, the well-designed CuZPMn@CpG protected CpG from nuclease degradation and overcame the electrostatic barrier of the cell membrane, leading to a significant enhancement in the cellular uptake upon NIR irradiation.

The *in vitro* immune-stimulatory activity of CuZPMn@CpG was evaluated with the secretion of Th1-polarizing cytokines, TNF-α, from RAW264.7 cells. TNF-α, as an indicator of immune response, was tested by enzyme-linked immunosorbent assay. CuZPMn@CpG induced the production of TNF-α significantly compared to free CpG (Fig. 4B) because of the low nuclease degradation and high cellular uptake of CuZPMn@CpG. Moreover, CuZPMn NCs without CpG also triggered the secretion of TNF-α to some extent by Mn^{2+} ions produced from the partial dissolution of the MnO_2 layer.[33] The amount of TNF-α secreted with NIR irradiation was approximately 2-fold higher than that without NIR irradiation. The disintegration of

CuZPMn@CpG under NIR irradiation achieved a remarkable release of CpG additionally because of the burst of the NCs. The CpG encapsulated in ZIF-8 during its preparation and that without the protection of the PDA layer were also tested for comparison to reveal the high immune activation of CpG wrapped on the ZIF-8 surface (ESI Fig. S9†).

Synergic therapy and *in vitro* cytotoxicity assay

Cytotoxicity was used to confirm the *in vitro* synergic therapeutic efficiency of different composites by 3-(4,5-dimethylthiazol-2-yl)-2,5-diphenyltetrazolium bromide (MTT) assay using 4T1 cells as a model (Fig. 4C). The survival rate of 4T1 cells treated with CuZPMn was greater than 90% even at 200 μg mL^{-1}. Such high biosafety was reported owing to the low toxicity of the precursors of the composites. After loading of PpIX and CpG, the composites still showed low cytotoxicity. Thus, CpG alone can't induce the apoptosis of 4T1 cells without invoking the antigen presenting cells, and PpIX is biocompatible (ESI Fig. S10A†). In contrast, the groups treated with PDT, PTT, and chemotherapy exhibited significant cell death in a concentration-dependent manner. The highest cytotoxicity was observed for the synergic therapy of PDT–PTT–chemotherapy–immunotherapy with cell viability less than 2% at the 200 μg mL^{-1} level (Fig. 4C).

To reveal the therapeutic mechanism and effect of immunotherapy, an upper-and-lower-chamber Transwell system was used for RAW264.7-4T1 cells co-cultured to mimic the *in vivo* tumor microenvironment (Fig. 4D). The upper chamber of RAW264.7 cells incubated with CuZPMn@CpG was subjected to 808 nm irradiation for 3 min to trigger the release of CpG to achieve the immunotherapy. 3 min NIR irradiation was perfect for the collapse of the NCs, but not sufficient to induce the photothermal apoptosis of RAW264.7. After being co-cultured with RAW264.7 cells, the viability of 4T1 cells decreased from 91% to 70% at the 200 μg mL^{-1} level (Fig. 4C). Thus, the CuZPMn@CpG invoked effectively the immune activity of RAW264.7 cells to secrete cytokine TNF-α for the apoptosis of cancer cells.[32]

The chemotherapy group treated with CuZPMn@DOX showed lower cell toxicity than that treated with free DOX (ESI Fig. S10B†), because it was difficult to release DOX without NIR irradiation. The viability of 4T1 cells was remarkably inhibited after irradiation with an 808 nm laser, far beyond the additive result achieved by the combination of chemotherapy and PTT (ESI Fig. S10C†). The additive therapeutic effect of CuZPMn@DOX with NIR irradiation was measured by multiplying the cell mortality rate of CuZPMn@DOX and CuZPMn + NIR. The attractive cancer cell killing ability of CuZPMn@DOX + NIR was attributed to the synergistic effect of chemotherapy and PTT, in combination with the effective NIR-triggered DOX release. The results of cytotoxicity assay and the synergic efficiency demonstrated that the NCs were biocompatible, and the intrinsic and synergistic therapeutic properties were clearly revealed.

GSH-responsive T_1-weighted MR imaging and biodistribution and excretion of CuZPMn NCs

Glutathione (GSH), as an endogenous antioxidant, is overexpressed in cancer cells. GSH can effectively reduce non-MR-active MnO_2 to MR-active Mn^{2+} ions for "turn-on" T_1-weighted MR imaging. Fig. 4E shows that CuZPMn exhibited an excellent GSH-activated "turn-on" T_1-weighted MRI effect as the T_1 signal was enhanced obviously compared to that without GSH (inset of Fig. 4E). The longitudinal relaxivity value (r_1) was only 0.6 mM^{-1} s^{-1} and became 8.8 mM^{-1} s^{-1} in the presence of GSH, two-fold higher than that of commercial Gd-DTPA (3.7 mM^{-1} s^{-1}) and free $MnCl_2$ (4.3 mM^{-1} s^{-1}) (ESI Fig. S11†).[34] The released Mn^{2+} ions chelated with hydrophilic PDA and altered the ^1H relaxivity of water with increasing rotational correlation time for MR signal enhancement.[35] After injecting CuZPMn into a tumor-bearing mouse intravenously, the tumor site was brightened and became the brightest at 10 h post-injection due to effective reduction of MnO_2 by GSH under the tumor microenvironment (Fig. 4F). Thus, CuZPMn is promising for GSH-activated "turn-on" MRI guided multi-modality therapy with high sensitivity.

The biodistribution of CuZPMn *in vivo* was studied by analyzing the Mn content in the tissues at different time points post injection (ESI Fig. S12†). At 10 h post injection, the Mn content in tumors reached a maximum of 12.1%, indicating the high accumulation of the NCs at tumor sites owing to the EPR effect; the outcome is beneficial for anticancer applications.[36] The high accumulation of CuZPMn in the liver and spleen was observed because of the strong phagocytosis in the reticuloendothelial system.[37] Furthermore, a high content of Mn was also detected in feces of mice after the injection of CuZPMn, demonstrating the excretion of CuZPMn (ESI Fig. S13†).

In vivo antitumor efficiency

The *in vivo* antitumor efficiency of CuZPMn@PpIX/DOX/CpG was tested with a clinically relevant therapeutic setting with 4T1 tumor-bearing mice as models. Treatments for all groups were repeated every 3 days over 18 days, including intravenous injection, PDT and PTT irradiation. Tumor sizes were monitored (Fig. 5A and B). Tumor growth was remarkably inhibited in the CuZPMn@PpIX treated group with 655 nm excitation for

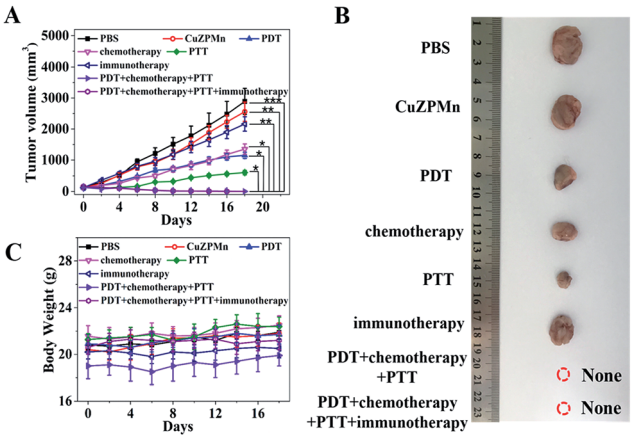

Fig. 5 (A) Tumor size and (B) photographs of excised tumors after different treatments with PBS as a negative control and CuZPMn as a positive control. (C) Body weight trend of the mice after different treatments.

PDT, the CuZPMn@DOX treated group for chemotherapy, and the CuZPMn treated group with 808 nm excitation for PTT. Either PDT, chemotherapy, or PTT itself exhibited an inhibitory effect on tumor growth. However, immunotherapy alone cannot inhibit the tumor, similar to previous results which indicated that immunotherapy was invalid for large solid tumors.[38] PDT–chemotherapy–PTT and PDT–chemotherapy–PTT–immunotherapy presented superior therapeutic efficiency. The tumors were totally eliminated owing to their synergistic effect. Moreover, the body weights of all groups remained normal without any noticeable decrease (Fig. 5C). No appreciable sign of organ damage or inflammatory lesions was observed after different treatments, as revealed by the hematoxylin and eosin (H&E) staining images of the major organs (ESI Fig. S14†).

In vivo anti-recurrence and anti-lung metastasis efficacy evaluation

To investigate the immune activation ability of the nanocomposites, induced tumor recurrence and lung metastasis experiments were conducted. For the anti-recurrence efficacy study, 1×10^7 4T1 tumor cells suspended in 100 μL sterile PBS were subcutaneously injected into the left hind limb of the mice on the fifth day after finishing the treatments with PBS, PDT–chemotherapy–PTT and PDT–chemotherapy–PTT–immunotherapy, respectively (Fig. 6A). The PDT–chemotherapy–PTT group showed a slower recurrence compared with the PBS group, possibly because of the insufficient immune response from CuZPMn@PpIX/DOX (Fig. 6B and C).[16] The solid tumor of the PDT–chemotherapy–PTT treatment group was ablated completely, the same as that of the PDT–chemotherapy–PTT–immunotherapy group in the initial therapy. However, the latter was totally recurrence-free after 4T1 tumor cells were re-injected into the mice.

For the anti-lung metastasis model, 4T1 tumor cells (1×10^7 cells) were intravenously injected into the mice on the fifth day after finishing the treatments with PBS, PDT–chemotherapy–PTT and PDT–chemotherapy–PTT–immunotherapy (Fig. 6A). Then, the body weight was monitored and that of the PBS group was found to have decreased dramatically as shown in Fig. 6D. We further photographed the lung of the mice after stained with India ink (Fig. 6E). The lungs became severely swollen and stiff and lung metastasis of cancer spots occurred heavily in the PBS-treated mice. The white tumorous nodes appeared in the PDT–chemotherapy–PTT group, suggested that PDT–chemotherapy–PTT is incapable of eradicating lung metastasis. However, no lung metastasis was observed when introducing immunotherapy to activate the immune system of the mice treated with PDT–chemotherapy–PTT–immunotherapy.[39] This was further confirmed with H&E staining of the lungs (Fig. 6F). The results of anti-lung metastasis were consistent with those of the anti-recurrence study of tumors. Thus, our innovative "all-in-one" composites not only eliminated primary solid tumors with the synergic effect of PDT, PTT, and chemotherapy, but also consolidated the therapeutic effect to inhibit the recurrence and metastasis of tumors through the long-term immune response of CpG.

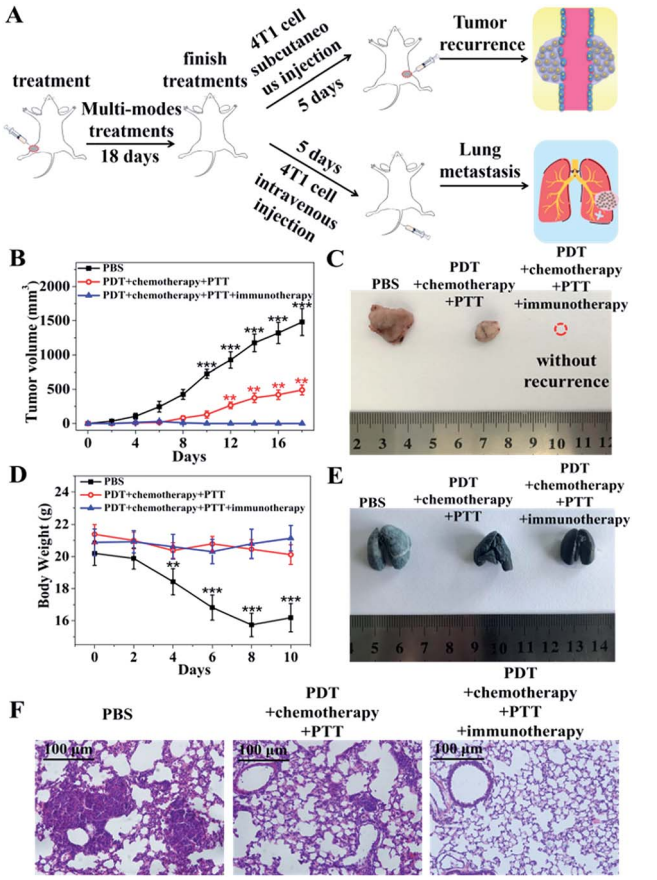

Fig. 6 (A) Schematic illustration of the anti-recurrence and anti-lung metastasis study with CuZPMn@PpIX/DOX/CpG as the probe. (B) Volumes and (C) photographs of the tumors for induced tumor recurrence of the mice after initial treatments with PBS, PDT–chemotherapy–PTT, and PDT–chemotherapy–PTT–immunotherapy. (D) Body weights, (E) photographs of the India ink-treated lungs and (F) H&E staining of lung tissues of the mice after 4T1 tumor cells were intravenously injected into the PBS, PDT–chemotherapy–PTT and PDT–chemotherapy–PTT–immunotherapy treated groups.

Conclusions

In summary, we developed a versatile one-pot multi-drug loading strategy based on ZIF-8 for elimination of solid tumors and anti-recurrence/metastasis. Agents of photothermal-, photodynamic-, and chemo-therapy were well combined in the nanomedicine for their complementary advantages to achieve a synergistic treatment effect. The high photothermal conversion efficiency of CuS nanoparticles triggered burst drug release for a high curative effect. The multi-drug co-loading and NIR-triggered drug release method eliminated the problems of tedious loading, limited capacity, and slow and uncontrollable drug release. Moreover, the recurrence/metastasis of tumors was effectively inhibited by the potent immunological memory induced by CpG, which was simply adsorbed on the positive surface of ZIF-8. The "all-in-one" system provided a versatile drug loading strategy to combine multi-modality therapy according to clinical needs and holds great promise as an efficient nanomedicine for multi-modality therapy of cancer without recurrence/metastasis for clinical application.

All animal experimental protocols were approved by the Institutional Animal Care Committee of Nankai University and all methods were carried out in accordance with the relevant guidelines and regulations from the Institutional Animal Care Committee of Nankai University, China.

Conflicts of interest

There are no conflicts to declare.

Acknowledgements

This work was supported by the National Natural Science Foundation of China (No. 21435001 and 21675090) and the National Basic Research Program of China (973 Program, No. 2015CB932001).

Notes and references

1 J. C. Yang, Y. Chen, Y. H. Li and X. B. Yin, *ACS Appl. Mater. Interfaces*, 2017, **9**, 22278–22288.
2 G. X. Lv, W. S. Guo, W. Zhang, T. B. Zhang, S. Y. Li, S. Z. Chen, A. S. Eltahan, D. L. Wang, Y. Q. Wang, J. C. Zhang, P. C. Wang, J. Chang and X. J. Liang, *ACS Nano*, 2017, **10**, 9637–9645.
3 Y. P. Li, T.-Y. Lin, Y. Luo, Q. Q. Liu, W. W. Xiao, W. C. Guo, D. Lac, H. Y. Zhang, C. H. Feng, W. Hogiu, J. H. Walton, S. R. Cherry, D. J. Rowland, D. Kukis, C. X. Pan and K. S. Lam, *Nat. Commun.*, 2014, **5**, 4712.
4 Z. F. Ma, M. C. Zhang, X. D. Jia, J. Bai, Y. D. Ruan, C. Wang, X. P. Sun and X. Jiang, *Small*, 2016, **12**, 5477–5487.
5 J. Bai, X. Jia, W. Zhen, W. Cheng and X. Jiang, *J. Am. Chem. Soc.*, 2018, **140**, 106–109.
6 X. Liu, H. Sun, W. Shi, Y. Liu, Y. Sun and D. Ge, *Biomaterials*, 2018, **167**, 177–190.
7 D. L. Sheng, T. Z. Liu, L. M. Deng, L. Zhang, X. L. Li, J. Xu, L. Hao, P. Li, H. T. Ran, H. R. Chen and Z. G. Wang, *Biomaterials*, 2018, **165**, 1–13.
8 D. Yang, J. T. Xu, G. X. Yang, Y. Zhou, H. J. Ji, H. T. Bi, S. L. Gai, F. He and P. P. Yang, *Chem. Eng. J.*, 2018, **344**, 363–374.
9 M. X. Wu and Y. W. Yang, *Adv. Mater.*, 2017, **29**, 1606134.
10 A. C. McKinlay, P. K. Allan, C. L. Renouf, M. J. Duncan, P. S. Wheatley, S. J. Warrender, D. Dawson, S. E. Ashbrook, B. Gil, B. Marszalek, T. Duren, J. J. Williams, C. Charrier, D. K. Mercer, D. K. Mercer, S. J. Teat and R. E. Morris, *APL Mater.*, 2014, **2**, 124108.
11 B. Illes, S. Wuttke and H. Engelke, *Nanomaterials*, 2017, **7**, 351.
12 H. Q. Zheng, Y. N. Zhang, L. F. Liu, W. Wan, P. Guo, A. M. Nystrom and X. D. Zou, *J. Am. Chem. Soc.*, 2016, **138**, 962–968.
13 R. N. Wang, Y. Han, B. Sun, Z. Q. Zhao, Y. Opoku-Damoah, H. Cheng, H. Q. Zhang, J. P. Zhou and Y. Yang, *Small*, 2018, **14**, 1703110.
14 C. Wang, S. Q. Chen, Q. Yu, F. Q. Hu and H. Yuan, *J. Mater. Chem. B*, 2017, **5**, 2068–2073.
15 T. Holler, J. Theriault, R. J. Payne, J. Clark, S. Eski and J. L. Freeman, *J. Oncol.*, 2009, **2009**, 650340.
16 Q. Chen, L. G. Xu, C. Liang, C. Wang, R. Peng and Z. Liu, *Nat. Commun.*, 2016, **7**, 13193.
17 J. Xu, L. G. Xu, C. Y. Wang, R. Yang, Q. Zhuang, X. Han, Z. L. Dong, W. W. Zhu, R. Peng and Z. Liu, *ACS Nano*, 2017, **11**, 4463–4474.
18 J. B. Pan, Y. Q. Wang, C. Zhang, X. Y. Wang, H. Y. Wang, J. J. Wang, Y. Z. Yuan, X. Wang, X. J. Zhang, C. S. Yu, S. K. Sun and X. P. Yan, *Adv. Mater.*, 2018, **30**, 1704408.
19 Q. S. Han, X. H. Wang, X. H. Jia, S. F. Cai, W. Liang, Y. Qin, R. Yang and C. Wang, *Nanoscale*, 2017, **9**, 5927–5934.
20 A. V. Kroll, R. H. Fang, Y. Jiang, J. R. Zhou, X. L. Wei, C. L. Yu, J. Gao, B. T. Luk, D. Dehaini, W. W. Gao and L. F. Zhang, *Adv. Mater.*, 2017, **29**, 1703969.
21 L. Yan, X. F. Chen, Z. G. Wang, X. J. Zhang, X. Y. Zhu, M. J. Zhou, W. Chen, L. B. Huang, V. A. Roy, P. K. N. Yu, G. Y. Zhu and W. J. Zhang, *ACS Appl. Mater. Interfaces*, 2017, **9**, 32990–33000.
22 J. J. Liu, Z. Luo, J. X. Zhang, T. T. Luo, J. Zhou, X. J. Zhao and K. Y. Cai, *Biomaterials*, 2016, **83**, 51–65.
23 D. Zucker, D. Marcus, Y. Barenholz and A. Goldblum, *J. Controlled Release*, 2009, **139**, 73–80.
24 M. Hembury, C. Chiappini, S. Bertazzo, T. L. Kalber, G. L. Drisko, O. Ogunlade, S. Walker-Samuel, K. S. Krishna, C. Jumeaux, P. Beard, C. S. R. Kumar, A. E. Porter, M. F. Lythgoe, C. Boissiere, C. Sanchez and M. M. Stevens, *Proc. Natl. Acad. Sci. U. S. A.*, 2015, **112**, 1959–1964.
25 X. Hu, X. D. Liu, X. D. Zhang, H. X. Chai and Y. M. Huang, *Biosens. Bioelectron.*, 2018, **105**, 65–70.
26 Y. Zhang, C. Q. Liu, F. M. Wang, Z. Liu, J. S. Ren and X. G. Qu, *Chem. Commun.*, 2017, **53**, 1840–1843.
27 Z. F. Wang, X. J. Tang, X. X. Wang, D. D. Yang, C. Yang, Y. B. Lou, J. X. Chen and N. Y. He, *Chem. Commun.*, 2016, **52**, 12210–12213.
28 G. B. Yang, L. G. Xu, Y. Chao, J. Xu, X. Q. Sun, Y. F. Wu, R. Peng and Z. Liu, *Nat. Commun.*, 2017, **8**, 902.
29 J. J. Liu, Q. Chen, W. W. Zhu, X. Yi, Y. Yang, Z. L. Dong and Z. Liu, *Adv. Funct. Mater.*, 2017, **27**, 1605926.
30 E. Latz, A. Schoenemeyer, A. Visintin, K. A. Fitzgerald, B. G. Monks, C. K. Knetter, E. Lien, N. J. Nilsen, T. Espevik and D. T. Golenbock, *Nat. Immunol.*, 2004, **5**, 190–198.
31 F. Duan, X. C. Feng, X. J. Yang, W. T. Sun, Y. Jin, H. F. Liu, K. Ge, Z. H. Li and J. C. Zhang, *Biomaterials*, 2017, **122**, 23–33.
32 Y. Zhang, Z. F. Cui, H. T. Kong, K. Xia, L. Pan, J. Li, Y. H. Sun, J. Y. Shi, L. H. Wang, Y. Zhu and C. H. Fan, *Adv. Mater.*, 2016, **28**, 2699–2708.
33 Y. Tao, M. Li, J. S. Ren and X. G. Qu, *Chem. Soc. Rev.*, 2015, **44**, 8636–8663.
34 Y. Yang, W. J. Zhu, Z. L. Dong, Y. Chao, L. Xu, M. W. Chen and Z. Liu, *Adv. Mater.*, 2017, **29**, 1703588.
35 W. T. Yang, W. S. Guo, W. J. Le, G. X. Lv, F. H. Zhang, L. Shi, X. L. Wang, J. Wang, S. Wang, J. Chang and B. B. Zhang, *ACS Nano*, 2016, **10**, 10245.

36 W. Song, J. Kuang, C. X. Li, M. K. Zhang, D. W. Zheng, X. Zeng, C. J. Liu and X. Z. Zhang, *ACS Nano*, 2018, **12**, 1978–1989.
37 X. Liu, N. Huang, H. Li, H. Wang, Q. Jin and J. Ji, *ACS Appl. Mater. Interfaces*, 2014, **8**, 5657–5668.
38 Z. Z. Wang, Y. Zhang, Z. Liu, K. Dong, C. Q. Liu, X. Ran, F. Pu, E. G. Ju, J. S. Ren and X. G. Qu, *Nanoscale*, 2017, **9**, 14236–14247.
39 J. R. Peng, Y. Xiao, W. T. Li, Q. Yang, L. W. Tan, Y. P. Jia, Y. Qu and Z. Y. Qian, *Adv. Sci.*, 2018, **5**, 1700891.